Supplemental Document

optica

Electron dynamics in laser-driven atoms near the continuum threshold: supplement

Mingqing Liu,[1,†] Songpo Xu,[2,3,†] Shilin Hu,[4] Wilhelm Becker,[5,6] Wei Quan,[2,3,8] Xiaojun Liu,[2,3,9] and Jing Chen[1,7,10]

[1] *Institute of Applied Physics and Computational Mathematics, Beijing 100088, China*
[2] *State Key Laboratory of Magnetic Resonance and Atomic and Molecular Physics, Wuhan Institute of Physics and Mathematics, Innovation Academy for Precision Measurement Science and Technology, Chinese Academy of Sciences, Wuhan 430071, China*
[3] *University of Chinese Academy of Sciences, Beijing 100049, China*
[4] *Guangdong Provincial Key Laboratory of Quantum Metrology and Sensing & School of Physics and Astronomy, Sun Yat-Sen University (Zhuhai Campus), Zhuhai 519082, China*
[5] *Max-Born-Institut, Max-Born-Strasse 2a, 12489 Berlin, Germany*
[6] *National Research Nuclear University MEPhI, Kashirskoe Shosse 31, 115409 Moscow, Russia*
[7] *Shenzhen Key Laboratory of Ultraintense Laser and Advanced Material Technology, Center for Advanced Material Diagnostic Technology, and College of Engineering Physics, Shenzhen Technology University, Shenzhen 518118, China*
[8] *e-mail: charlywing@wipm.ac.cn*
[9] *e-mail: xjliu@wipm.ac.cn*
[10] *e-mail: chen_jing@iapcm.ac.cn*
[†] *These authors contributed equally to this work.*

Supplement DOI: https://doi.org/10.6084/m9.figshare.14460123

Parent Article DOI: https://doi.org/10.1364/OPTICA.418636

Electron dynamics in laser-driven atoms near the continuum threshold: supplemental document

This supplemental document shows the details of the experimental setup, the quantum model, comparison between theoretical calculation and experimental measurement, and the analysis of the phase difference between different trajectories.

1. EXPERIMENTAL SETUP

The experiments have been performed with a home-made velocity-map imaging (VMI) spectrometer with a base pressure of the interaction chamber maintained around 10^{-9} mbar. The 1800 nm femtosecond laser beam with a 55-fs pulse duration is generated from an optical parametric amplifier pumped by a commercial Ti:sapphire laser system with a repetition rate of 1 kHz. The laser-pulse energy is precisely controlled with a combination of a broadband achromatic $\lambda/2$ plate and a thin-film polarizer. Before being introduced into the spectrometer, the laser beam at 1800 nm passes through an optical aperture with a diameter D of 4.0 mm and a 100-mm focal-length planoconvex lens. The beam waist, w_0, and the Rayleigh length, z_R, are estimated to be 45 μm and 3534 μm, respectively (see, e.g., [1]). A collimated supersonic beam of atomic Ar intersects the laser beam at the focal spot. Excited Ar atoms (with principal quantum numbers $n \leq 75$) and ions Ar^+ produced in the interaction of the laser field and the supersonic atomic beam are detected by a position-sensitive Microchannel Plate (MCP) detector equipped with a delay-line anode (DLD80 RoentDek Handels GmbH). See Ref. [2] for more experimental details.

Note that, to perform reliable intensity-dependent measurements of the RSE yields, it is important to keep the laser-intensity uncertainty as low as possible. In our measurement, special efforts were made to reduce the influence of laser-intensity fluctuation [2]. In detail, during the data acquisition, the laser-pulse energy was measured by a photodiode and recorded shot-by-shot by a home-made integration circuit. This circuit can transfer the measured pulse-energy signal to a delayed NIM signal, which is recorded by a computer along with the Ar^* signal for each laser pulse. In the off-line analysis, only the data with pulse energies in a small range are chosen to produce the spectra. In this way, the influence of the pulse-to-pulse intensity fluctuation can be significantly reduced and the laser-intensity fluctuation can be controlled to be around 1.7% at 1800 nm.

2. THE QUANTUM MODEL

The RSE capture probability with the electron initially in the state $|\Psi_i\rangle$ is given by $P = \sum_{nlm} |M_{nlm}|^2$, with

$$M_{nlm} = \lim_{t\to\infty}(-i)^2 \int_{-\infty}^{t} d\tau' \int_{-\infty}^{\tau'} d\tau \left\langle \Psi_{nlm}(t) \left| U\left(t,\tau'\right) V U_V\left(\tau',\tau\right) H_I(\tau) \right| \Psi_i(\tau) \right\rangle \tag{S1}$$

where $U\left(t,\tau'\right)$ denotes the total time-evolution operator with the Coulomb and the laser fields and $U_V\left(\tau',\tau\right)$ the Volkov time-evolution operator. The operator H_I represents the interaction between the electron and the laser field and V denotes the Coulomb potential. In the limit $t \to \infty$, the final state $\langle \Psi_{nlm}(t)|U\left(t,\tau'\right)$ can be approximated by the field-dressed Rydberg state

$$\Psi^d_{nlm}(\boldsymbol{r},\tau') = \psi_{nlm}(\boldsymbol{r}) e^{-iE_n\tau'} e^{i\boldsymbol{r}\cdot\boldsymbol{A}(\tau')} e^{-i\int_{-\infty}^{\tau'} d\tau A^2(\tau)/2}, \tag{S2}$$

which approximately satisfies the time-dependent Schrödinger equation (TDSE). The state $\psi_{nlm}(\boldsymbol{r})$ is a field-free Rydberg state corresponding to the energy level $E_n = -Z/(2n^2)$, and the principal, angular-momentum, and magnetic quantum numbers are n, l, and m, respectively. The times τ and τ' denote the instants of ionization and capture, respectively. More details can be found in Ref. [3].

After the approximation $\langle \Psi_{nlm}(t)|U\left(t,\tau'\right)| \rightarrow \langle \Psi^d_{nlm}(\tau')|$, Eq. (S1) does not reproduce the modulation of the intensity-dependent excitation probability as it was calculated by the TDSE

for 1800 nm pulse [4] and is shown in Fig. 2(b) of the main text. We attempt to improve the description by taking rescattering into account with the help of the Dyson equation

$$U\left(t,\tau'\right) = U_V\left(t,\tau'\right) - i\int_{\tau'}^{t} d\tau'' U(t,\tau'') V U_V\left(\tau'',\tau'\right). \tag{S3}$$

Inserting Eq. (S3) into Eq. (S1) yields

$$M_{nlm} = \lim_{t\to\infty}(-i)^2\int_{-\infty}^{t} d\tau' \int_{-\infty}^{\tau'} d\tau \left\langle \Psi_{nlm}(t)\left|U_V\left(t,\tau'\right) V U_V\left(\tau',\tau\right) H_I(\tau)\right|\Psi_i(\tau)\right\rangle \tag{S4}$$

$$+ \lim_{t\to\infty}(-i)^3\int_{-\infty}^{t} d\tau' \int_{-\infty}^{\tau'} d\tau \int_{\tau'}^{t} d\tau'' \left\langle \Psi_{nlm}(t)\left|U\left(t,\tau''\right) V U_V\left(\tau'',\tau'\right) V U_V\left(\tau',\tau\right) H_I(\tau)\right|\Psi_i(\tau)\right\rangle. \tag{S5}$$

Here, the first term (S4) describes the direct transition from an intermediate Volkov state to a field-free highly excited final state. This term disappears in the limit of t going to infinity since the Volkov propagator $U_V(t,\tau') \propto (t-\tau')^{-3/2}$ (see Eq. (7) of Ref. [3]) goes to zero when $t \gg T_p$ (Note that $t \geq \tau' \geq \tau$ and the integration over τ is restricted to the pulse length T_p). The same argument does not apply to the second term (S5) because rather than the Volkov propagator $U_V(t,\tau'')$ it displays the complete propagator $U(t,\tau'')$. This contains the Coulomb propagator $U_0(t,\tau'')$, which does not spread as $(t-\tau'')^{-3/2}$.

We approximate the second term (S5) of the RSE transition amplitude with rescattering included by

$$\begin{aligned} M_{nlm} =& (-i)^3\int_{-\infty}^{\infty} d\tau' \int_{-\infty}^{\tau'} d\tau \int_{\tau'}^{\infty} d\tau'' \int d^3\boldsymbol{p}\int d^3\boldsymbol{k} \\ & \times \langle \Psi^d_{nlm}(\tau'')|V|\Psi^{(V)}_{\boldsymbol{p}}(\tau'')\rangle\langle\Psi^{(V)}_{\boldsymbol{p}}(\tau')|V|\Psi^{(V)}_{\boldsymbol{k}}(\tau')\rangle\langle\Psi^{(V)}_{\boldsymbol{k}}(\tau)|H_I|\Psi_i(\tau)\rangle, \end{aligned} \tag{S6}$$

where, as above, we introduced the field-dressed Rydberg state $\langle\Psi^d_{nlm}(\tau'')|$. The momenta after and before rescattering, respectively, are denoted by $\boldsymbol{p}$ and $\boldsymbol{k}$. The intermediate Volkov state is $|\Psi^{(V)}_{\boldsymbol{k}}\rangle$, which is a solution of the TDSE without taking the Coulomb potential into account. It can be written as (in length gauge)

$$|\Psi^{(V)}_{\boldsymbol{k}}(\boldsymbol{r},t)\rangle = \frac{1}{(2\pi)^{3/2}} e^{i[\boldsymbol{k}+\boldsymbol{A}(t)]\cdot\boldsymbol{r}} e^{-i\int_{-\infty}^{t} d\tau[\boldsymbol{k}+\boldsymbol{A}(\tau)]^2/2}. \tag{S7}$$

Equation (S6) can be rewritten as

$$M_{nlm} = \frac{(-i)^3}{(2\pi)^6}\int_{-\infty}^{\infty} dt_r \int_{-\infty}^{t_r} dt_i \int_{t_r}^{\infty} dt_c \int d^3\boldsymbol{p}\int d^3\boldsymbol{k}\; V_{nlm,\boldsymbol{p}} V_{\boldsymbol{p},\boldsymbol{k}} V_{\boldsymbol{k}+\boldsymbol{A}(t_i),i}\; e^{iS(\boldsymbol{p},\boldsymbol{k},t_i,t_r,t_c)}, \tag{S8}$$

where

$$V_{nlm,\boldsymbol{p}} = \langle\psi_{nlm}(\boldsymbol{r}_1)| - \frac{Z}{|\boldsymbol{r}_1|}|e^{i\boldsymbol{p}\cdot\boldsymbol{r}_1}\rangle, \tag{S9}$$

$$V_{\boldsymbol{p},\boldsymbol{k}} = \langle e^{-i\boldsymbol{p}\cdot\boldsymbol{r}_2}| - \frac{Z}{|\boldsymbol{r}_2|}|e^{i\boldsymbol{k}\cdot\boldsymbol{r}_2}\rangle, \tag{S10}$$

$$V_{\boldsymbol{k}+\boldsymbol{A}(t_i),i} = \langle e^{-i[\boldsymbol{k}+\boldsymbol{A}(t_i)]\cdot\boldsymbol{r}_3}|\boldsymbol{r}_3\cdot\boldsymbol{E}(t_i)|\psi_i(\boldsymbol{r}_3)\rangle. \tag{S11}$$

The integration variables t_i, t_r, and t_c can be interpreted as the instants of ionization, rescattering, and capture, respectively. The initial state is $\psi_i(\boldsymbol{r})$, and the electric field can be described by $\boldsymbol{E}(t) = E_0\sin\omega t\hat{\boldsymbol{e}}_z$ and its vector potential $\boldsymbol{A}(t) = -\int_{-\infty}^{t}\boldsymbol{E}(\tau)d\tau$, where E_0 is the peak intensity and $\hat{\boldsymbol{e}}_z$ an unit polarization vector. The field-free Rydberg states are given by

$$\begin{aligned} \psi_{nlm}(\mathbf{r}) &= N_{nl}R_{nl}(r)Y_{lm}(\theta,\varphi), \\ N_{nl} &= \frac{(2\kappa_n)^{3/2}}{\Gamma(2l+2)}\sqrt{\frac{\Gamma(n+l+1)}{2n\Gamma(n-l)}}, \\ R_{nl}(r) &= (2\kappa_n r)^l e^{-\kappa_n r}\,{}_1F_1(-n+l+1,2l+2,2\kappa_n r), \end{aligned} \tag{S12}$$

where $\kappa_n = Z/n$, $Y_{lm}(\theta,\varphi)$ is a spherical harmonic, and ${}_1F_1(x,y,z)$ the confluent hypergeometric function. The action is

$$S(\boldsymbol{p},\boldsymbol{k},t_i,t_r,t_c) = \frac{1}{2}\int_{-\infty}^{t_c} dt\boldsymbol{A}^2(t) + E_n t_c - \frac{1}{2}\int_{t_r}^{t_c} dt[\boldsymbol{p}+\boldsymbol{A}(t)]^2 - \frac{1}{2}\int_{t_i}^{t_r} dt[\boldsymbol{k}+\boldsymbol{A}(t)]^2 + I_p t_i \quad \text{(S13)}$$

with I_p the ionization energy.

For $l \neq 0$ the density of the Rydberg state has two centers at $\mathbf{r}^+_{nlm} \equiv \mathbf{r}_{nlm}$ and $\mathbf{r}^-_{nlm} = -\mathbf{r}^+_{nlm} \equiv -\mathbf{r}_{nlm}$ (see Fig. S1(a) and Ref. [3]). Therefore, we decompose the Rydberg-state wave function as

$$\psi_{nlm}(\mathbf{r}) = \psi_{nlm+}(\mathbf{r}) + \psi_{nlm-}(\mathbf{r}). \quad \text{(S14)}$$

The functions $\psi_{nlm\pm}(\mathbf{r})$ are concentrated around $\mathbf{r} = \pm\mathbf{r}_{nlm}$ and satisfy $\psi_{nlm-}(-\mathbf{r}) = (-1)^l\psi_{nlm+}(\mathbf{r})$. Writing $\psi_{nlm+}(\boldsymbol{r}) = \psi_{nlm+}(\boldsymbol{r}-\boldsymbol{r}_{nlm}+\boldsymbol{r}_{nlm}) \equiv \tilde{\psi}_{nlm}(\boldsymbol{\rho})$, where $\boldsymbol{\rho} = \boldsymbol{r}-\boldsymbol{r}_{nlm}$, we obtain [3]

$$V_{nlm,\boldsymbol{p}} = -\int d^3\boldsymbol{\rho}\frac{1}{|\boldsymbol{\rho}+\boldsymbol{r}_{nlm}|}\tilde{\psi}^*_{nlm}(\boldsymbol{\rho})\left[e^{i\boldsymbol{p}\cdot\boldsymbol{\rho}}e^{i\boldsymbol{p}\cdot\boldsymbol{r}_{nlm}} + (-1)^l e^{-i\boldsymbol{p}\cdot\boldsymbol{\rho}}e^{-i\boldsymbol{p}\cdot\boldsymbol{r}_{nlm}}\right]. \quad \text{(S15)}$$

For the saddle-point evaluation, we associate the exponentials $\exp(\pm i\boldsymbol{p}\cdot\boldsymbol{r}_{nlm})$ with the action and disregard the $\boldsymbol{p}$ dependence of $\exp(\pm i\boldsymbol{p}\cdot\boldsymbol{\rho})$. That is, we determine the variables t_i, t_r, t_c, $\boldsymbol{k}$ and $\boldsymbol{p}$ so that the action $S \pm \boldsymbol{p}\cdot\boldsymbol{r}_{nlm}$ is stationary. This yields the saddle-point equations (see, e.g. [3, 5, 6])

$$\frac{1}{2}[\boldsymbol{k}+\boldsymbol{A}(t_i)]^2 = -I_p, \quad \text{(S16)}$$

$$[\boldsymbol{k}+\boldsymbol{A}(t_r)]^2 = [\boldsymbol{p}+\boldsymbol{A}(t_r)]^2, \quad \text{(S17)}$$

$$\boldsymbol{A}^2(t_c)/2 + E_n = [\boldsymbol{p}+\boldsymbol{A}(t_c)]^2/2, \quad \text{(S18)}$$

$$\boldsymbol{k} = -\frac{1}{t_r-t_i}\int_{t_i}^{t_r} dt\boldsymbol{A}(t), \quad \text{(S19)}$$

$$\boldsymbol{p} = -\frac{1}{t_c-t_r}\int_{t_r}^{t_c} dt\boldsymbol{A}(t) \pm \frac{\mathbf{r}_{nlm}}{t_c-t_r}. \quad \text{(S20)}$$

Equations (S16), (S17), and (S18) describe, respectively, energy conservation in the tunneling, scattering, and capture processes. Equation (S19) determines the intermediate electron momentum, while Eq. (S20) takes into account that the electron is captured at one of the two positions $\pm\boldsymbol{r}_{nlm}$. The solutions $(t_i, t_r, t_c, \boldsymbol{p}, \boldsymbol{k})$ of Eqs. (S16)–(S20) define the quantum orbits for specified n, l, and m.

For forward scattering, we have $\boldsymbol{p} = \boldsymbol{k}$, and Eq. (S17) is satisfied for all values of t_r. For specified $\boldsymbol{p}$, the solution of Eq. (S16) for the time t_i is known in analytical form [6]:

$$2\cos^2(\mathrm{Re}\,\omega t_i) = 1+\gamma^2+\delta^2-\sqrt{Q}, \quad \text{(S21)}$$

$$\cosh(\mathrm{Im}\,\omega t_i) = -\delta\frac{\cos\theta}{\cos(\mathrm{Re}\,\omega t_i)}. \quad \text{(S22)}$$

Here θ is the electron emission angle with respect to the laser polarization axis, $\gamma = \sqrt{I_p/(2U_p)}$ is the Keldysh parameter [7], $\delta = \sqrt{E_p/(2U_p)}$, $Q = (1+\gamma^2+\delta^2)^2 - 2\delta^2[1+\cos(2\theta)]$, and U_p is the ponderomotive energy for a linearly polarized laser field. For forward scattering, the emission angle in the lab frame is $\theta = 0$ or $\theta = \pi$. Then, the solution for the rescattering time t_r is obtained from Eq. (S16):

$$p\omega(t_r-t_i)/A_0 + \sin\omega t_r - \sin\omega t_i = 0, \quad \text{(S23)}$$

where $A_0 = E_0/\omega$. From Eq. (S21) we obtain $\mathrm{Re}\,t_i/T > 0.25$, which guarantees that the electron can revisit the ionic core after tunneling. In this paper, the ionization time t_i is confined to the interval $0 \le t_i \le 6T$ and the pulse duration is $10T$ so that we can calculate the capture process up to $\mu = 4$ (see Section 5 of supplemental document for the definition of μ). For a short-range potential, forward scattering is weak. In contrast, for a Coulomb potential, the matrix element in Eq. (S10) is $\langle e^{-i\boldsymbol{p}\cdot\boldsymbol{r}_2}|-\frac{Z}{|\boldsymbol{r}_2|}|e^{i\boldsymbol{k}\cdot\boldsymbol{r}_2}\rangle \propto Z/(\boldsymbol{p}-\boldsymbol{k})^2$, which for forward scattering is divergent. It has to be regularized by introducing the ionization rate of the ground state [8].

3. COMPARISON BETWEEN THEORETICAL CALCULATION AND EXPERIMENTAL MEASUREMENT

Based on the experimental efforts mentioned above, in Fig. S1, the measured [solid lines] and calculated [dashed lines] intensity dependence of the yields of the Rydberg states (Ar^*) and ion (Ar^+) at 1800 nm are presented. For the measurements, a prominent sequence of steps with a period of about 50 TW/cm^2 can be identified in the intensity dependence of the Ar^* yields. It is worth noting that the measured ionization yield is observed to saturate at about 270 TW/cm^2, while the measured excitation yield does not yet show saturation at this intensity. This is the reason of the rapid increase of the measured ratio Ar^*/Ar^+ in the high intensity regime as shown in Fig. 1(b) of the main text. In fact, most of the Rydberg states quickly decay radiatively to the ground state and only a fraction of the Rydberg states decaying to a long-lived metastable state with an internal energy more than 10 eV can be detected by MCP detector. Considering that the yield of Rydberg atoms is lower by orders of magnitude than that of the ions, the density of the Ar supersonic beam has to be maintained high enough for a good signal-to-noise ratio of the Rydberg atoms. Thus, if the laser intensity is too strong, the ion yields could be too high for our MCP detector to respond linearly with respect to the ion numbers and the detection efficiency would begin to saturate. As shown in Fig. S1, for laser intensity higher than 270 TW/cm^2, the detection efficiency already saturates. Note that the saturation intensity for the detector could be lower than that of the single ionization of Ar (the ionization yield saturates at about 330 TW/cm^2 for 800 nm laser with a similar pulse duration as shown in Fig. 4(b) of Ref. [2]). Meanwhile, the calculated excitation yield after volume averaging also shows oscillation structure with a period of about 50 TW/cm^2, in good agreement with the experimental data including the locations of the minima. Focal-volume averaging for yields of Ar^* and Ar^+ is performed by Eq. (B11) in Ref. [2] for super-Gaussian beam with $n = 2.6$. The ionization yield is calculated by the SFA theory without considering saturation. Note that the focal-averaged calculated Ar^* shown in Fig. S1 is multiplied by a factor of 2.4 for better comparison with the experiment.

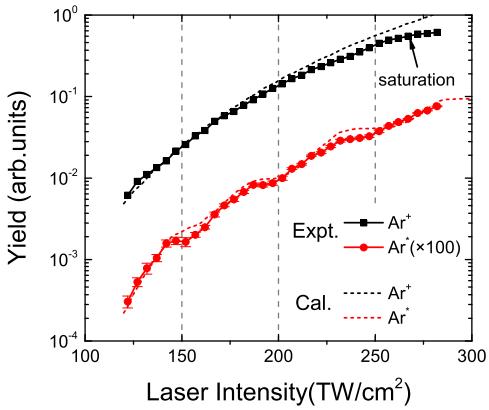

Fig. S1. Measured intensity dependence of the yield of ions Ar^+ and excited atoms Ar^*, which is multiplied by a factor of 100 to make the minima more noticeable, and corresponding calculated results after volume averaging are shown for comparison. The yields of Ar^+ and excited atoms Ar^* are calculated by the SFA theory and the quantum model, respectively.

4. CAPTURE REGION OF THE RYDBERG WAVE FUNCTION

As in the semiclassical analysis of Ref. [3], the capture region in this paper is defined by the condition that $|\psi|^2 \geq 0.8|\psi|^2_{\max}$ where $|\psi|^2$ [see Eq. (S12)] is the density of the Rydberg wave function with its maximum $|\psi|^2_{\max}$. In Fig. S2(a), we show the density of the final Rydberg state [9,8,0] ($n = 9, l = 8, m = 0$) in the $x - z$ plane. The z-direction range that satisfies the above capture criterium is 50 a.u. $\leq z \leq$ 90 a.u. and -90 a.u. $\leq z \leq -50$ a.u., i. e., $R_c = 40$ a.u.

The capture region size R_c increases with increasing principal quantum number n. Since this is dependent on the wavelength ($n \propto E_0^{1/2}\lambda$), R_c shows a wavelength scaling of about $\lambda^{1.1}$ for the most populated Rydberg state as displayed in Fig. S2(b).

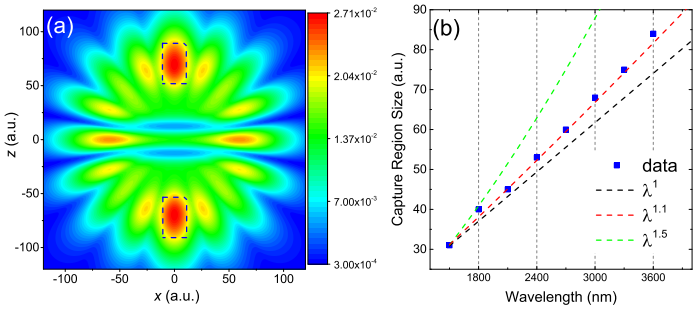

Fig. S2. Spatial density distribution of the Rydberg state [9,8,0] ($n = 9, l = 8, m = 0$) in the $x - z$ plane. The two blue rectangles delineate the spatial capture region. (b): Wavelength dependence of the capture region size R_c.

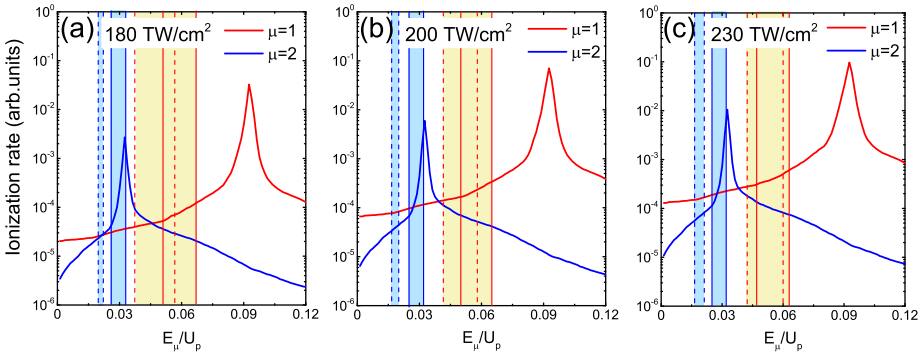

Fig. S3. The LES energy spectra (solid lines) for $\mu = 1$ (red) and $\mu = 2$ (blue) for (a): 180 TW/cm^2, (b): 200 TW/cm^2, (c): 230 TW/cm^2 at 1800 nm wavelength, for the same final Rydberg state, Moreover, each panel displays the energy regions for the trajectories that can be recaptured by the final Rydberg state [9,8,0]. For recapture at $z > 0$ (50 a.u. $< z <$ 90 a.u.) they are bounded by solid vertical lines (red for $\mu = 1$ and blue for $\mu = 2$) and shaded in the corresponding color. For capture at $z < 0$ (-50 a.u. $> z >$ -90 a.u.) the capture regions are bounded by dashed lines.

5. ELECTRON TRAJECTORIES CONTRIBUTING TO THE RSE

According to the analysis of Ref. [6], the solutions for the forward-scattering time come in pairs, which are denoted by the index $\mu = 0, 1, 2, 3, ...$ with increasing $t_r - t_i$. The solutions with $\mu = 0$ do not contribute neither to the LES nor to RSE, but generate a smooth background. Thus both the LES and the oscillation structure in RSE come from trajectories with $\mu > 0$.

In order to compare the energy range of the electrons that contribute to RSE for different intensities at specific wavelength, the LES energy spectra of $\mu = 1$ and $\mu = 2$ for three intensities at 1800 nm are displayed in Fig. S3. From an analysis as presented in Fig. 3 of the main text, we see from Fig. S3(a) that these energy ranges at 180 TW/cm^2 are $0.051 \leq E_\mu/U_p \leq 0.067$ for $\mu = 1$ and $0.026 \leq E_\mu/U_p \leq 0.033$ for $\mu = 2$, both for recapture at $z > 0$. The energy ranges for capture at $z < 0$ are also presented and indicated by the rectangular regions bounded by the vertical dashed lines. Likewise, at 230 TW/cm^2 in Fig. S3(c), the corresponding energy ranges for $\mu = 1$ and $\mu = 2$ are $0.047 \leq E_\mu/U_p \leq 0.063$ and $0.024 \leq E_\mu/U_p \leq 0.032$, respectively, and similarly in Fig. S3(b) at 200 TW/cm^2. This demonstrates that the energy ranges of the electrons contributing to RSE slightly shift to lower energies with increasing intensity for fixed wavelength.

6. WAVELENGTH DEPENDENCE OF THE OSCILLATION PERIOD OF THE RSE PROBABILITY

According to Fig. 3(e) of the main text, the oscillation period of the RSE probability mainly depends on the intensity dependence of the phase difference between the recaptured $\mu = 1$ and $\mu = 2$ LES trajectories. For trajectories considered in Figs. 3(a)-3(c) of the main text, both $\mu = 1$ and $\mu = 2$ LES trajectories with maximal weight are captured in the $z > 0$ region. Hence, using Eqs. (S19)-(S20), the phase of the amplitude for capture at the position $\pm\mathbf{r}_{nlm}$ is

$$\begin{aligned} &S(\boldsymbol{p}, \boldsymbol{k}, t_i, t_r, t_c) \pm \boldsymbol{p} \cdot \mathbf{r}_{nlm} \\ &= E_n t_c + I_p t_i + \frac{1}{2}\int_{-\infty}^{t_i} dt A^2(t) - \frac{p^2}{2}(t_c - t_r) - \boldsymbol{p} \cdot \left(\int_{t_r}^{t_c} dt \boldsymbol{A}(t) \mp \boldsymbol{r}_{nlm}\right) - \frac{k^2}{2}(t_r - t_i) - \boldsymbol{k} \cdot \int_{t_i}^{t_r} dt \boldsymbol{A}(t) \\ &= E_n t_c + I_p t_i + \frac{1}{2}\int_{-\infty}^{t_i} dt A^2(t) + \frac{p^2}{2}(t_c - t_r) + \frac{k^2}{2}(t_r - t_i). \end{aligned} \tag{S24}$$

For the field $A(t) = A_0 \cos \omega t$ and for forward scattering ($\boldsymbol{p} = \boldsymbol{k}$) this is

$$S = E_n t_c + I_p t_i + U_p t_i + \frac{U_p}{2\omega} \sin 2\omega t_i + \frac{p^2}{2}(t_c - t_i) \tag{S25}$$

with the ponderomotive energy $U_p = A_0^2/4$.

We now follow the semiclassical analysis of Ref. [3]. The LES energies E_μ ($\mu = 1, 2, \dots$) are given by the forward-scattering solutions ($\mathbf{p} = \mathbf{k}$) such that the ionization and rescattering times satisfy

$$\omega t_i = \frac{\pi}{2} + \omega\tau, \tag{S26}$$

$$\omega t_r = \frac{\pi}{2} + 2\pi\left(\mu + \frac{1}{2}\right) - \omega\tau, \tag{S27}$$

with the same $\tau \equiv \tau_\mu > 0$, which is independent of the laser intensity. The LES energies then are $E_\mu = p_\mu^2/2$, $p_\mu = -A(t_i) = A_0 \sin \omega\tau_\mu$ so that $E_\mu/U_p \approx 2\omega^2\tau_\mu^2$, since $\omega\tau_\mu \ll 1$ [6].

The graphical construction employed in Ref. [6] can be utilized to show that if an electron on an LES trajectory is to be recaptured at the position $\mathbf{r}_{nlm}$, then the time $t_c > t_r$ has to satisfy

$$\omega t_c = \frac{\pi}{2} + 2\pi\left(\mu + \frac{3}{2}\right) - \omega\tau. \tag{S28}$$

with the same τ as above. LES solutions that allow for recapture at a specified position only exist for a set of discrete intensities. Since, however, the recapture condition $|\psi|^2 \geq 0.8|\psi|^2_{\max}$ of Sec. 4 in supplemental document allows for recapture within a range of width R_c, there will be solutions within certain intensity ranges.

Recall that E_n denotes the energy of the Rydberg state. Since we are only interested in the intensity dependence of the phase difference for $\mu = 1$ and $\mu = 2$, we drop the first two terms of the phase (S25), which are independent on the laser intensity. Using Eqs. (S26)-(S28) we obtain up to third order in $\omega\tau \ll 1$

$$\Delta S = S(\mu = 1) - S(\mu = 2) \equiv 2\pi C U_p/\omega \tag{S29}$$

where

$$C = 5\omega^2(\tau_1^2 - \tau_2^2) - 2\omega^2\tau_2^2 - \frac{5}{3\pi}\omega^3(\tau_1^3 - \tau_2^3). \tag{S30}$$

For 1800 nm, the energies of the trajectories with the maximal weights for $\mu = 1$ and $\mu = 2$ are $0.065U_p$ and $0.032U_p$, respectively. The corresponding $\omega\tau_1$ and $\omega\tau_2$ are 0.18 and 0.13, respectively, resulting in $C = 0.045$. Then, a change of the phase difference ΔS by 2π corresponds to an intensity change of $\Delta I = 50.4\ \mathrm{TW/cm^2}$, which is in good agreement with the calculated oscillation period of the RSE probability.

The quiver amplitude R_q of the electron in the laser field is proportional to the square of the laser wavelength λ, i.e., $R_q = E_0/\omega^2 \propto \sqrt{I}\lambda^2$, where I is the laser intensity. On the other hand, as shown in section 4 of this supplemental document, the size R_c of the capture region increases with increasing principal quantum number n and shows a wavelength scaling of about $\lambda^{1.1}$ for the most populated Rydberg state [see Fig. S2(b)]. As a result, the energy range of the electrons

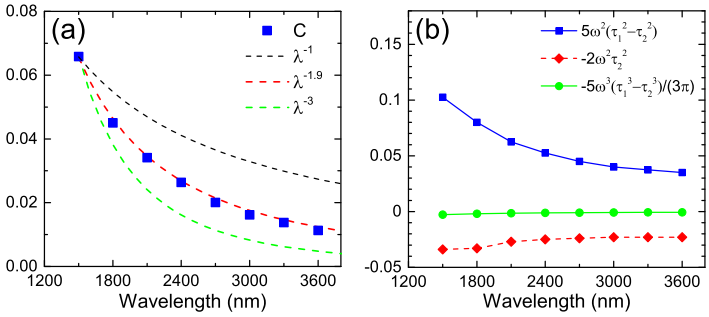

Fig. S4. (a): Wavelength dependence of the factor C. (b): Wavelength dependence of the three terms that make up the factor C.

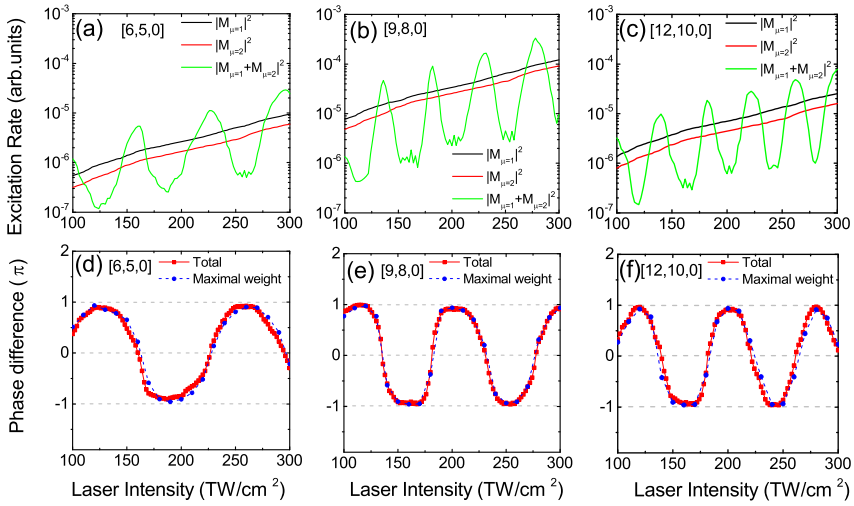

Fig. S5. Calculated intensity dependence of the RSE probabilities corresponding to $\mu = 1$ and $\mu = 2$ as well as their coherent sum at 1800 nm for the final Rydberg state (a): [6,5,0], (b): [9,8,0] and (c): [12,10,0]. Intensity dependence of the phase difference between the RSE amplitudes for $\mu = 1$ and $\mu = 2$ and that between two trajectories with the maximal weights of each μ for the final Rydberg state (d): [6,5,0], (e): [9,8,0] and (f): [12,10,0].

that contribute to RSE shrinks and shifts to lower energies with increasing laser wavelength [compare Fig. 3(c) and Fig. 3(b) in the text]. According to our calculation, the factor C exhibits a wavelength scaling of about $\lambda^{-1.9}$ as shown in Fig. S4(a). Therefore, the oscillation period scales with the wavelength as $\Delta I \propto \lambda^{-3} C^{-1} \propto \lambda^{-1.1}$, in agreement with the numerical-calculation result of $\lambda^{-1.2}$ presented in Fig. 4(b) of the main text. In addition, the dominant term of the factor C is $5(\omega^2\tau_1^2 - \omega^2\tau_2^2)$ as shown in Fig. S4(b), which is proportional to the energy difference between the two capture trajectories with the maximal weights. We conclude that the oscillation period of the RSE probability is mainly dependent on the above-mentioned energy difference.

Similar to Fig. 3(d) and Fig. 3(e) in the main text, we plot the RSE probabilities corresponding to $\mu = 1$ and $\mu = 2$ and their coherent sum at 1800 nm for the final Rydberg states [6,5,0] and [12,10,0], as well as their phase difference as a function of the laser intensity together with that of [9,8,0] in Fig. S5. Clearly, for the Rydberg states [6,5,0] and [12,10,0] the effect of the interference is similar to that of [9,8,0], and the oscillation period decreases as n increases. This is because with increasing n, the capture region moves away from the core, so that the energies of the capture trajectories having the maximal weights for $\mu = 1$ increase. However, for $\mu = 2$, the energy of the capture trajectories with the maximal weights changes much more slowly. So the energy difference between the two capture trajectories with the maximal weights increases as n increases, giving rise to an increase of the factor C and a decrease of the oscillation period of

the RSE probability. Hence, the results of Fig. S5 agree with the prediction of Eq. (S29). It should be mentioned that although the oscillation period changes with n, the oscillation period of the entire RSE probability is mainly determined by the Rydberg state [9,8,0], which dominates in the intensity range discussed in this paper.

REFERENCES

1. K. Thyagarajan and A. Ghatak, *Lasers: fundamentals and applications*, 2nd ed. (Springer US, 2011).
2. S. P. Xu, M. Q. Liu, S. L. Hu, Z. Shu, W. Quan, Z. L. Xiao, Y. Zhou, M. Z. Wei, M. Zhao, R. P. Sun, Y. L Wang, L. Q. Hua, C. Gong, X. Y. Lai, J. Chen, and X. J. Liu, "Observation of a transition in the dynamics of strong-field atomic excitation," Phys. Rev. A **102**, 043104 (2020).
3. S. L. Hu, X. L. Hao, H. Lv, M. Q. Liu, T. X. Yang, H. F. Xu, M. X. Jin, D. J. Ding, Q. G. Li, W. D. Li, W. Becker, and J. Chen, "Quantum dynamics of atomic Rydberg excitation in an intense laser field," Opt. Express **27**, 31629-31643 (2019).
4. B. Piraux, F. Mota-Furtado, P. F. O'Mahony, A. Galstyan, and Yu. V. Popov, "Excitation of Rydberg wave packets in the tunneling regime," Phys. Rev. A **96**, 043403 (2017).
5. W. Becker, F. Grasbon, R. Kopold, D. B. Milošević, G. G. Paulus, and H. Walther, "Above-threshold ionization: From classical features to quantum effects," Adv. At. Mol. Opt. Phys. **48**, 35-98 (2002).
6. W. Becker, S. P. Goreslavski, D. B. Milošević, and G. G. Paulus, "Low-energy electron rescattering in laser-induced ionization," J. Phys. B: At. Mol. Opt. Phys. **47**, 204022 (2014).
7. L. V. Keldysh, "Ionization in the field of a strong electromagnetic wave," Sov. Phys. JETP **20**, 1307-1314 (1965).
8. L. Guo, S. S. Han, X. Liu, Y. Cheng, Z. Z. Xu, J. Fan, J. Chen, S. G. Chen, W. Becker, C. I. Blaga, A. D. DiChiara, E. Sistrunk, P. Agostini, and L. F. DiMauro, "Scaling of the low-energy structure in above-threshold ionization in the tunneling regime: theory and experiment," Phys. Rev. Lett. **110**, 013001 (2013).